Computer Modeling in Engineering & Sciences

Tech Science Press

https://doi.org/10.32604/cmes.2026.080866

ARTICLE

Computer Modeling and Characterization of Plastic Strain Hardening in Ti-6Al-4V under Tension and Compression

Teng Long[1], **Leyu Wang**[2,*], **James D. Lee**[3] **and Cing-Dao Kan**[2]

[1]Department of Mechanical and Materials Engineering, University of Cincinnati, Cincinnati, OH, USA
[2]Center for Collision Safety and Analysis, George Mason University, Fairfax, VA, USA
[3]Department of Mechanical and Aerospace Engineering, George Washington University, Washington, DC, USA

*Corresponding Author: Leyu Wang. Email: lwang28@gmu.edu

Received: 17 February 2026; Accepted: 15 May 2026; Published: 27 July 2026

ABSTRACT: Titanium alloy Ti-6Al-4V has been widely applied in many industries, for example, aerospace, marine, automotive, and biomedical engineering systems, where accurate characterization of plastic deformation is important for evaluating material performance and potential failure under severe loading conditions. This material shows non-linear plasticity and tension–compression asymmetry, which makes the strain hardening characterization important for computational failure analysis and crashworthiness-related simulations. However, conventional strain hardening models and parameter identification methods often rely on linear or extrapolation-based assumptions and are sensitive to initial guesses due to the non-convex nature of the optimization problem. In this study, a flexible rational-polynomial-based strain-hardening model was employed to characterize the stress–strain responses of Ti-6Al-4V under both tensile and compressive loading. To identify the polynomial parameters, an online hyperparameter tuning Bayesian optimization framework was adopted. The finite element predictions closely reproduce the experimental force–displacement responses under both tensile and compressive loading. This consistency demonstrates the capability of the proposed data-driven computational framework to identify strain-hardening parameters and characterize the plastic deformation behavior of Ti-6Al-4V alloy.

KEYWORDS: Titanium alloy; strain hardening; plasticity; Bayesian optimization; hyperparameter tuning

1 Introduction

Titanium alloy Ti-6Al-4V is widely applied in aerospace [1], marine [2], automotive [3], biomedical [4], etc., because of its excellent strength [5,6], corrosion resistance [5,7], fatigue [8] performance. The plastic deformation behavior is complex and it has been extensively investigated using plane-strain compression [9] and impact-related simulations such as bird-strike [10], ballistic impact [11] studies, etc. [12]. Consequently, accurate material modeling of Ti-6Al-4V is essential for structurally reliable design, forming processes, impact, crashworthiness, etc. In these applications, plastic strain hardening plays a crucial role in modeling severe deformation to capture the extreme mechanical behaviors in numerical analysis [13,14].

Experimental investigations have demonstrated that Ti-6Al-4V shows nonlinear plasticity and tension–compression asymmetry [15–17]. As a result, simple linear hardening laws are insufficient to describe its deformation behavior in plasticity. In previous studies, different advanced material models for Ti-6Al-4V have been proposed including Hill yield function [18], exponential-extrapolated-based hardening laws [15], Hansel–Spittel model [19], Johnson-Cook material model [20], etc., to describe the strain hardening of Ti-6Al-4V in either tension [15,18] or compression [15,19,20]. Although the number of material parameters in these models is generally of the same order as that of the polynomial-based formulation in this study, many existing approaches rely on extrapolation-based strategies [15,18,20] or piecewise linear descriptions [19] in the quasi-static region. In contrast, the rational-polynomial-based model provides a compact and continuous representation for the hardening response. This offers greater fitting flexibility over a large strain range and can capture complex nonlinear stress–strain behavior more effectively. In other words, the main contribution of the present study does not lie in reducing the number of parameters, but rather in improving the capability to accurately fit strain-hardening behavior in both tension and compression within a unified phenomenological framework.

Conventionally, the material parameter identification process of Ti-6Al-4V relies on grid search [18], response surface [19], gradient-based [20], evolutionary [21] optimizations. While these methods are effective in certain cases, they are often highly sensitive to initial parameter guesses and require a large number of iterations to address the nonlinear and non-convex optimization tasks. To overcome these limitations, Bayesian optimization, as a global optimization strategy, especially for high computational cost problems, becomes a better solution [22]. It works well in the non-convex parameter space to avoid the suboptimal solutions. Bayesian optimization is a powerful and data-efficient approach that can determine the next parameter by considering all the previous information. By using its acquisition function, this approach can decide the most promising next parameter set in a smart way that balances exploration and exploitation. In addition, previous optimization for Ti-6Al-4V did not consider the effect of hyperparameter tuning during the optimization process. In the present work, Bayesian optimization is combined with an online Gaussian Process hyperparameter tuning scheme. This enables an adaptive feature and therefore provides a clear distinction from earlier studies [18–20].

To the best of our knowledge, a rational-polynomial-based strain-hardening model combined with Bayesian optimization and online hyperparameter tuning has not yet been applied to characterize the plastic deformation behavior of Ti-6Al-4V. Therefore, the objective of this study is to employ an in-house online hyperparameter Bayesian optimization framework [23] to identify the parameters of a polynomial-based strain-hardening model for Ti-6Al-4V. The model parameters are calibrated using previously reported tension and compression experimental data [12,15,17,24].

The remainder of this paper is organized as follows. The experimental procedures and corresponding finite element models are first introduced. Then, the material model and Bayesian optimization framework are described in detail. The curve fitting results between experiment and numerical simulations, together with the optimization history, are presented next. Finally, the key findings and implications of this study are discussed and summarized.

2 Method

The experiment reported by Hammer et al. [12] is first reviewed. The finite element model with the material model formulation is then presented. Finally, the optimization algorithm for material model parameter characterization is described in detail. Fig. 1 provides an overall and concise scheme of the workflow and highlights the connections among the subsections.

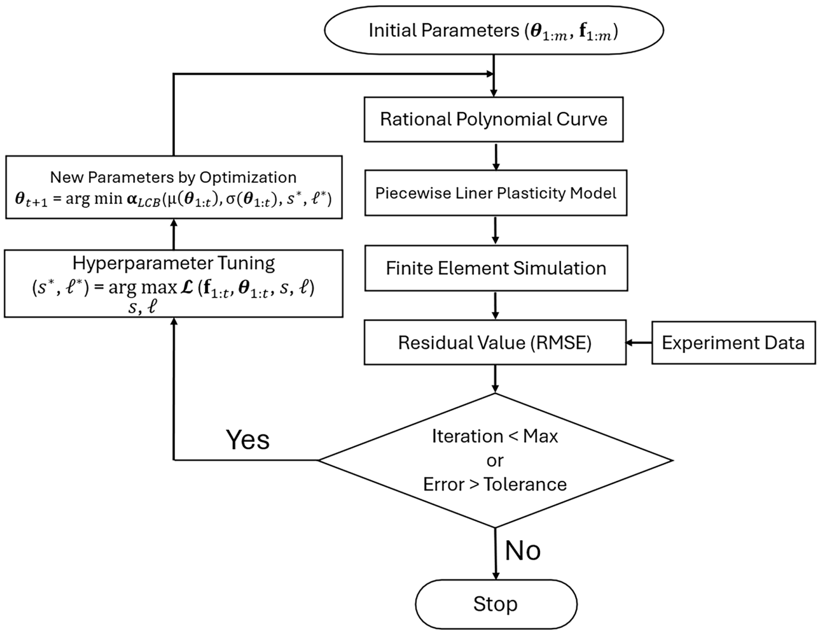

Figure 1: Flowchart for material model parameter characterization. Note: several numbers (m) of initial data sets for parameters and their residual values are needed to initialize the process.

2.1 Experiment

2.1.1 Specimen Preparation

Previous studies conducted material coupon tests on a 0.25-inch-thick Ti-6Al-4V plate to characterize its mechanical behavior under different material orientations, strain rates, and temperatures [12,15,17]. The quasi-static tests conducted at a strain rate of $1 \times 10^{-4}\ \mathrm{s}^{-1}$ in both tension and compression were selected for the present study. The mechanical property of Ti-6Al-4V was measured through the rolled direction according to Fig. 2. The additional specific raw material and specimen information are documented in Table 1.

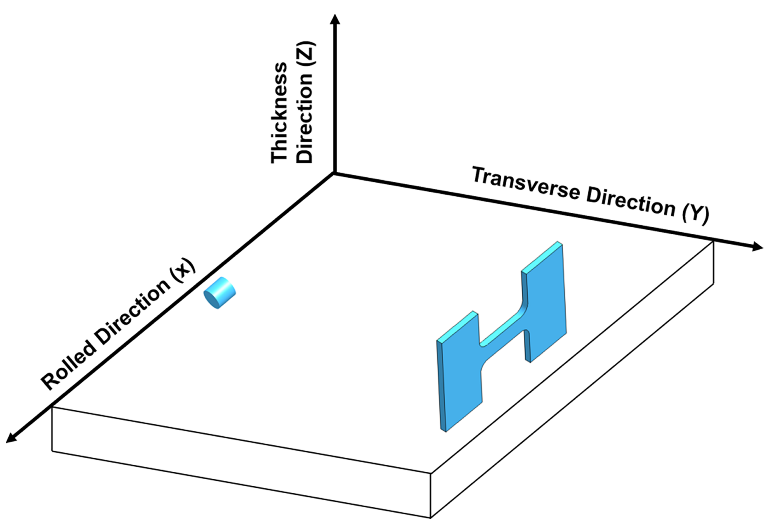

Figure 2: Orientation of specimen manufacturing [17,15].

Table 1: Experiment information for tension and compression [17,15]. Tension experiment ID: M2-TMT-P3-SG1-O1-SR1-T1-N1. Compression experiment ID: M2-TMC-P3-SG1-01-SR1-T1-N1.

Experiment	Plate Stock	Specimen Geometry	Specimen Orientation	Strain Rate (1/s)	Temperature (°C)
Tension	0.25	Flat dogbone	Rolled	1.0E−04	Room
Compression	0.25	Cylinder	Rolled	6.9E−05	Room

The tensile specimen was cut based on the profile shown in Fig. 3. Specifically, it was processed using the electrical discharge machine according to the dimensions in Table 2. The cylindrical specimen used for the compression test is shown in Fig. 4. Considering the buckling limitation in the experiment, the value of length over diameter was close to one. The raw material was cut and turned to the dimensions in Table 3.

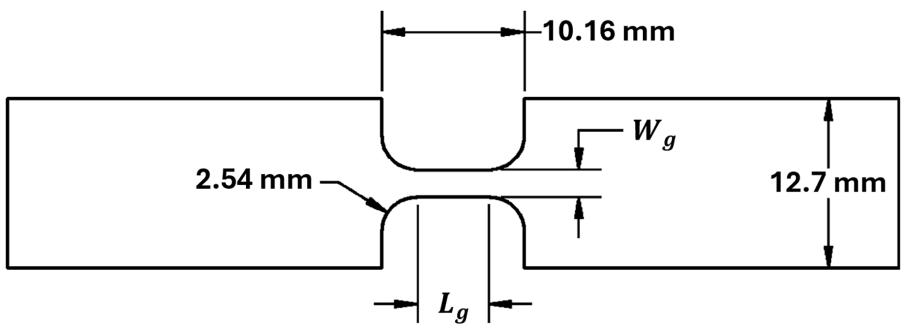

Figure 3: Tension specimen dimension for plane stress study [17,15].

Table 2: Tensile specimen dimension.

Length (L_g) (mm)	Gage Width (W_g) (mm)	Thickness (h) (mm)
5.0800	2.0650	0.7160

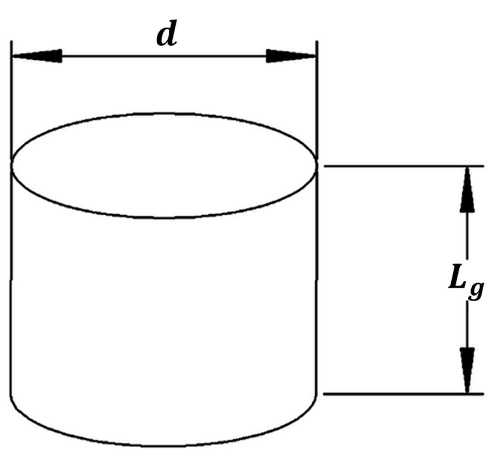

Figure 4: Compression experiment specimen.

Table 3: Compression specimen dimension.

Diameter (d) (mm)	Height (L_g) (mm)
3.8560	3.8227

2.1.2 Experiment Setup

The experimental setup [12] for the previously conducted test is summarized as follows: An INSTRON 1321 model biaxial servohydraulic machine was used for tension and compression tests. The MTS Flex Test SE controller controlled the testing platform and MTS 493.25 digital signal conditioner received the signal at 100 kHz. The linear variable differential transformer was used to measure the displacement for both tests. For compression, vascomax C-350 and tungsten carbide were inserted between the Inconel push rod surfaces and the specimen to protect the push rod from damage. To maintain the quasi-static loading for strain rate, with 1.0E−04 (1/s) and 6.9E−05 (1/s) for tension and compression, respectively. Note: The experimental data used in this study were adopted directly from the published government report [12]. Therefore, the present work focuses on the inverse finite element identification framework rather than on the experimental details.

2.2 Finite Element Modeling

Our finite element models were created based on the unit system: mm, ms, kg, kN, and GPa. LS-DYNA R16.1 double precision was used to solve the numerical models. The mesh sizes for both tension and compression are not larger than the Federal Aviation Administration report by Haight et al. [15]. In our tensile simulation, comparison with a refined mesh of approximately half the element size showed only about a 5% difference in the force–displacement response, which indicates that the present mesh is adequate for the calibration purpose of this work. For the compression simulation, the same nominal mesh size as the reference report was adopted. For both cases, hexahedral elements were adopted. For the compression model, a single-integration scheme with No. 6 hourglass control in LS-DYNA was used, whereas for the tension model, a fully integrated scheme without hourglass control was applied. Specifically, the element formulation was selected to ensure that the hourglass energy remained small compared with the total energy and therefore it maintains numerical stability. To only consider the elastic-plastic behavior, the model is designed to simulate a quasi-static process. A higher loading speed was applied to simulate the model in a reasonable time, since this is an explicit dynamic feature in LS-DYNA. The loading-speed convergence studies have been done to ensure the boundary conditions make sense. The smoothed displacement control boundary was used to avoid the oscillation at the beginning of the simulation.

The finite element models for the tensile test and compressive test are shown in Figs. 5 and 6, respectively. The prescribed boundary displacement condition was applied on the node set in red in the positive Z direction for the tensile test and negative Z in the compressive test, with a fixed boundary in both X and Y directions. The fixed boundaries were applied to the node set in green at the bottom. For the compression test, the upper and lower bottom plates were modeled using the real material in the experiment. For the tensile test, the red and green stars in the middle line are the nodes to be recorded in history, while in the compressive test, the node on the top surface in the center is for the displacement history. The force from the cross-section plane is labeled the purple line on the left side of Figs. 5 and 6.

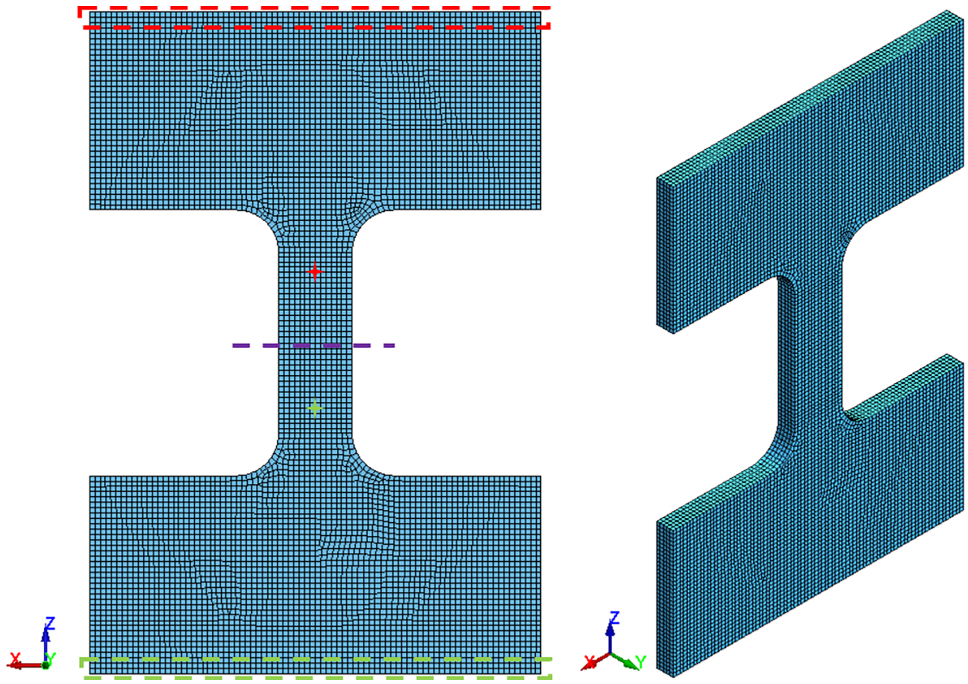

Figure 5: Tensile specimen finite element model. Left: Front view. Right: Iso view.

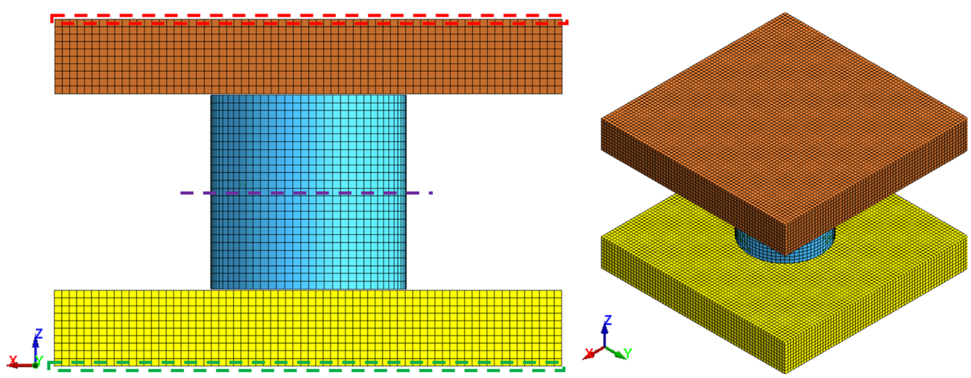

Figure 6: Compression specimen finite element model. Left: Front view. Right: Iso view.

Material Model

A piecewise plastic model, `*MAT_024` in LS-DYNA [25], was used in both the tension and compression finite element models. Elastic deformation material parameters were known as the fixed parameters (Tension: Young's modulus = 110 GPa and Poisson's ratio = 0.342. Compression: Young's modulus = 203 GPa and Poisson's ratio = 0.3) [15]. In plasticity, the rational polynomial in Eq. (1) was used to generate the strain hardening process [26]. There are five parameters with p_1, p_2, p_3 in the numerator and q_1, q_2 in the denominator to describe the relation using effective plastic strain, $\bar{\varepsilon}^p$, as inputs and yield stress, σ_Y, as output. In this work, the coefficients to be optimized are used to reproduce the hardening response to fit the force-displacement response. Thus, they do not individually correspond to direct physical quantities. The different signs and orders of magnitude reflect the mathematical structure of the polynomial.

$$\sigma_Y = \frac{p_1(\bar{\varepsilon}^p)^2 + p_2(\bar{\varepsilon}^p) + p_3}{(\bar{\varepsilon}^p)^2 + q_1(\bar{\varepsilon}^p) + q_2} \tag{1}$$

The yield stress, σ_Y, vs. effective plastic strain, $\bar{\varepsilon}^p$, is the required curve for the LCSS ins *MAT_024 in LS-DYNA (this one-dimensional curve can also be characterized using the uniaxial loading condition starting from the yield point). In LS-DYNA, this curve determines the slope H in the plasticity process or the return-mapping algorithm [25,27–30] from Eqs. (2) to (12). The names of variables are explained in Table 4.

Table 4: Variable definitions for the return-mapping algorithm. Note: The von Mises strength is also known as the initial yield stress (σ_0). The effective stress is also referred to as von Mises stress or equivalent stress.

Variable	**Description**
σ_Y	Yield stress
$\bar{\varepsilon}^p$	Effective plastic strain
H	Slope of yield stress vs. effective plastic strain curve
σ_{V0}	Von Mises strength, initial yield stress
$\boldsymbol{\xi}$	Shifted stress
$\boldsymbol{e}$	True strain
$\boldsymbol{t}$	Cauchy stress
$\boldsymbol{s}$	Deviatoric stress
$\boldsymbol{\beta}$	Back stress

In the return-mapping algorithm, the plasticity deformation process follows either (both) isotropic or (and) kinematic rules. Specifically, $c = 1$ means the pure isotropic hardening, while $c = 0$ makes kinematic hardening only. $0 < c < 1$ represents the isotropic and kinematic hardenings happen at the same time. At time step t_{n+1}, $\tilde{f}_{n+1}$ (the yield function trial value) is:

$$\tilde{f}_{n+1} = \left\|\tilde{\boldsymbol{\xi}}_{n+1}\right\| - \sqrt{\frac{2}{3}}\left(\sigma_{V0} + cH\bar{\varepsilon}_n^p\right) \tag{2}$$

where

$$\tilde{\mathbf{t}}_{n+1} = \lambda\,\mathrm{tr}\left(\mathbf{e}_{n+1} - \mathbf{e}_n^{\mathrm{p}}\right)\mathbf{I} + 2\mu\left(\mathbf{e}_{n+1} - \mathbf{e}_n^{\mathrm{p}}\right) \tag{3}$$

$$\tilde{\mathbf{s}}_{n+1} = \tilde{\mathbf{t}}_{n+1} - \frac{1}{3}\mathrm{tr}\left(\tilde{\mathbf{t}}_{n+1}\right)\mathbf{I} \tag{4}$$

$$\tilde{\boldsymbol{\xi}}_{n+1} \equiv \tilde{\mathbf{s}}_{n+1} - \boldsymbol{\beta}_n \tag{5}$$

During iteration for each time step, if $\tilde{f}_{n+1}$ (Eq. (2)) > 0, the following variables are updated. If it is not, we do not update the variables below.

$$\Delta\gamma = \frac{\tilde{f}_{n+1}}{2\mu + \frac{2}{3}H} \tag{6}$$

$$\mathbf{e}_{n+1}^{\mathrm{p}} = \mathbf{e}_n^{\mathrm{p}} + \Delta\gamma\frac{\tilde{\boldsymbol{\xi}}_{n+1}}{\left\|\tilde{\boldsymbol{\xi}}_{n+1}\right\|} \tag{7}$$

$$\boldsymbol{\beta}_{n+1} = \boldsymbol{\beta}_n + \frac{2}{3}(1-c)H\Delta\gamma\frac{\tilde{\boldsymbol{\xi}}_{n+1}}{\|\tilde{\boldsymbol{\xi}}_{n+1}\|} \tag{8}$$

$$\bar{\varepsilon}^p_{n+1} = \bar{\varepsilon}^p_n + \sqrt{\frac{2}{3}}\Delta\gamma \tag{9}$$

$$\mathbf{t}_{n+1} = \lambda\,\mathrm{tr}\left(\mathbf{e}_{n+1} - \mathbf{e}^{\mathrm{p}}_{n+1}\right)\mathbf{I} + 2\mu\left(\mathbf{e}_{n+1} - \mathbf{e}^{\mathrm{p}}_{n+1}\right) \tag{10}$$

$$\mathbf{s}_{n+1} = \mathbf{t}_{n+1} - \frac{1}{3}\mathrm{tr}\left(\mathbf{t}_{n+1}\right)\mathbf{I} \tag{11}$$

After the above variables from Eqs. (6) to (11) are updated, the value of the yield function returns to zero in Eq. (12), which has been proven in literature [26], the yield function value returns to zero as shown in Eq. (12), which has been proven in literature [26].

$$f_{n+1} = \left\|\mathbf{s}_{n+1} - \boldsymbol{\beta}_{n+1}\right\| - \sqrt{\frac{2}{3}}\left(\sigma_{V0} + cH\bar{\varepsilon}^p_{n+1}\right) = 0 \tag{12}$$

2.3 Optimization

The optimal parameters p_1, p_2, p_3, q_1, q_2 are needed to minimize the root mean squared error to obtain the best curve fit of force-displacement responses from finite element solution and experiment. In this study, Bayesian optimization as the global optimizer finds the parameters first. Then it is followed by a local search using the Nelder–Mead algorithm to further improve the results. In this study, we used our in-house Bayesian optimization program [23]. The implementation details of Bayesian optimization are presented below. There are two main steps in Bayesian optimization. (Step 1): constructing a Gaussian-process-based surrogate model. (Step 2): finding the target material parameters in the acquisition function. The Gaussian process can be defined by its prior mean m and covariance function k [31] using $\boldsymbol{\theta}$ and $\boldsymbol{\theta}'$ as input parameter vector (In this case, we have $\boldsymbol{\theta} = [p_1, p_2, p_3, q_1, q_2]$):

$$f\left(\boldsymbol{\theta}\right) \sim \mathcal{N}\left(m\left(\boldsymbol{\theta}\right), k\left(\boldsymbol{\theta}, \boldsymbol{\theta}'\right)\right). \tag{13}$$

In this study, we adopt the exponential covariance function in Eq. (14), where s denotes the signal variance of the Gaussian process and represents the typical amplitude of variation of the objective function around its mean over the parameter space, while the length-scale ℓ controls how rapidly the Gaussian-process prediction changes as the input variables, i.e., the material parameters, vary. It is shown as:

$$k = s^2 \exp\left(-\frac{1}{2}r^2\right), \tag{14}$$

where $r^2 = \left(\boldsymbol{\theta} - \boldsymbol{\theta}'\right)^T \boldsymbol{\Sigma}\left(\boldsymbol{\theta} - \boldsymbol{\theta}'\right)$ and the directional nature of the model is determined by the matrix $\boldsymbol{\Sigma}$. In general, as an anisotropic model, $\boldsymbol{\Sigma}$ is defined as:

$$\boldsymbol{\Sigma} = diag(\boldsymbol{l})^{-2} = \begin{bmatrix} \ell_1^{-2} & 0 & \dots & 0 \\ 0 & \ell_2^{-2} & \dots & 0 \\ \vdots & \dots & \ddots & \vdots \\ 0 & 0 & \dots & \ell_d^{-2} \end{bmatrix} \tag{15}$$

To simplify the model, in this study, an isotropic model was applied. Then matrix of $\boldsymbol{\Sigma}$ is reduced to Eq. (16). Specifically, in the isotropic case, all length-scale components are assigned to the same value ($\ell_1 = \ell_2 = \cdots = \ell_d = \ell$). Then $\boldsymbol{I}$ is the $d \times d$ identity matrix.

$$\mathbf{\Sigma} = l^{-2}\boldsymbol{I} \tag{16}$$

Without enough prior information, it is a general procedure to assume the prior mean as zero [32–35]. Then the vector form of joint Gaussian distribution [32,36,37] is:

$$\begin{bmatrix} \mathbf{f}_{1:t} \\ f_{t+1} \end{bmatrix} \sim \mathcal{N}\left(0, \begin{bmatrix} \mathbf{K} & \mathbf{k} \\ \mathbf{k}^T & k(\boldsymbol{\theta}_{n+1}, \boldsymbol{\theta}_{n+1}) \end{bmatrix}\right), \tag{17}$$

where

$$\mathbf{K} = \begin{bmatrix} k(\boldsymbol{\theta}_1, \boldsymbol{\theta}_1) & \ldots & k(\boldsymbol{\theta}_1, \boldsymbol{\theta}_t) \\ \vdots & \ddots & \vdots \\ k(\boldsymbol{\theta}_t, \boldsymbol{\theta}_1) & \ldots & k(\boldsymbol{\theta}_t, \boldsymbol{\theta}_t), \end{bmatrix}, \tag{18}$$

$$\mathbf{k} = \left[k(\boldsymbol{\theta}_{t+1}, \boldsymbol{\theta}_1) \quad k(\boldsymbol{\theta}_{t+1}, \boldsymbol{\theta}_2) \ldots k(\boldsymbol{\theta}_{t+1}, \boldsymbol{\theta}_t)\right]^T, \tag{19}$$

$$\mathbf{f}_{1:t} = \left[f(\boldsymbol{\theta}_1) \quad f(\boldsymbol{\theta}_2) \ldots f(\boldsymbol{\theta}_t)\right]^T, \tag{20}$$

$$f_{t+1} = f_{t+1}(\boldsymbol{\theta}_{t+1}). \tag{21}$$

Based on the Sherman-Morrison-Woodbury identity, the predicted distribution at a new parameter point $\boldsymbol{\theta}_{t+1}$ is obtained as [38]:

$$P\left(f_{t+1} | \mathbb{D}_{1:t}, \boldsymbol{\theta}_{t+1}\right) \sim \mathcal{N}\left(\mu\left(\boldsymbol{\theta}_{t+1}\right), \sigma^2\left(\boldsymbol{\theta}_{t+1}\right)\right), \tag{22}$$

where

$$\mu\left(\boldsymbol{\theta}_{t+1}\right) = \mathbf{k}^T\mathbf{K}^{-1}\mathbf{f}_{1:t}, \tag{23}$$

$$\sigma^2\left(\boldsymbol{\theta}_{t+1}\right) = k(\boldsymbol{\theta}_{t+1}, \boldsymbol{\theta}_{t+1}) - \mathbf{k}^T\mathbf{K}^{-1}\mathbf{k}, \tag{24}$$

and $\mathbb{D}_{1:t}$ is data observed in history during iterations.

To maintain the numerical inverse stability, the Cholesky decomposition [39] approach was employed by adding Eq. (17) with an identity matrix scaled by 1×10^{-4}.

The lower confidence bound (LCB) acquisition function is used to balance exploration and exploitation, as shown in Eq. (25), where κ is given with 0.5. Eq. (26) is the process to find the parameter vector $\boldsymbol{\theta} = [p_1, p_2, p_3, q_1, q_2]$ in this study.

$$\alpha_{LCB}(\boldsymbol{\theta}) = \mu\left(\boldsymbol{\theta}\right) - \kappa\sigma\left(\boldsymbol{\theta}\right), \tag{25}$$

$$\boldsymbol{\theta}_{t+1} = \text{argmin}\ \alpha_{LCB}\left(\mu\left(\boldsymbol{\theta}\right), \sigma\left(\boldsymbol{\theta}\right)\right). \tag{26}$$

To improve Bayesian optimization, hyperparameters were updated by maximizing the log marginal likelihood function as shown in Eq. (27). In this study, the amplitude scaling parameter, s, and the length scale, ℓ, are as Gaussian process hyperparameters [38] that control the behavior of the covariance function in Eq. (14). These hyperparameters were reestimated every five iterations as the inputs for Eq. (26).

$$\mathcal{L} = \log p\left(\mathbf{f}_{1:t} \mid \boldsymbol{\theta}_{1:t}, \ell, s\right) = -\frac{1}{2}\mathbf{f}^T\mathbf{K}^{-1}\mathbf{f} - \frac{1}{2}\log|\mathbf{K}| - \frac{n}{2}\log\left(2\pi\right). \tag{27}$$

The local optimization, Nelder-Mead simplex algorithm [40,41], was used to further refine the solution. The SciPy package [42] with a tolerance of 10^{-4} was used as the stopping criterion. The residual value was calculated by root mean square error (RMSE).

3 Result

3.1 Force vs. Displacement Response

The good corrections for both tension and compression are shown in Figs. 7 and 8. The force vs. displacement from experiment in solid line and simulation in dashed line demonstrate good fits except the yield regions in Fig. 8a. Figs. 7b and 8b present the yield stress vs. effective plastic strain. Fig. 8a for tension displays a nonlinear strain-hardening behavior characterized by a high initial hardening modulus and decreasing hardening modulus as effective plastic strain increases. However, the compression curve in the Fig. 8b demonstrates an approximately linear relationship between yield stress and effective plastic strain. This shows the difference between tension and compression for the yield stress and effective plastic strain relation. The stress-strain relations were plotted based on Eq. (1) using the parameters in Table 5.

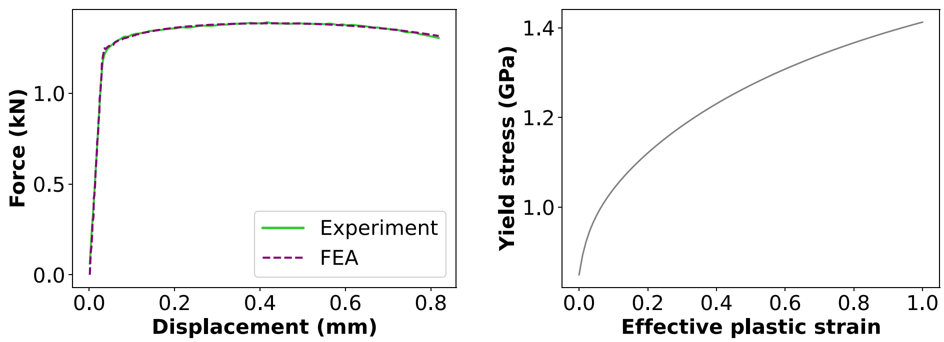

(**a**) (**b**)

Figure 7: Tensile specimen using the best fit by Bayesian optimization and Nelder-Mead simplex algorithms: (**a**) Force-displacement response; (**b**) Yield stress-effective plastic strain.

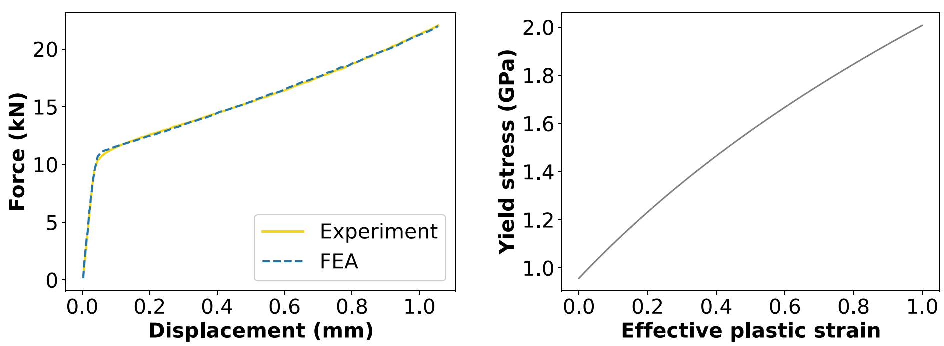

(**a**) (**b**)

Figure 8: Compressive specimen using the best fit by Bayesian optimization and Nelder-Mead simplex algorithms: (**a**) Force-displacement response; (**b**) Yield stress-effective plastic strain.

Table 5: Best-fit coefficients of the rational polynomial in Eq. (1), identified by Bayesian optimization with online hyperparameter tuning refined with Nelder-Mead simplex algorithm.

Specimen	p1	p2	p3	q1	q2
Tension	180,705.2853	99,165.1216	2702.9313	96,888.4937	3183.7165
Compression	−720,826.2347	3,151,373.7714	995,962.4396	1,095,715.8565	1,070,812.3241

3.2 Optimization Residual Value History

The residual value optimization histories for both tension and compression tests are shown in Fig. 9. This demonstrates that the Bayesian optimization scheme results in a good fit for force vs. displacement response using the material model in Eq. (1). The residual values significantly decrease using Bayesian optimization. This provides a good choice for a starting point for a local optimizer, Nelder-Mead simplex.

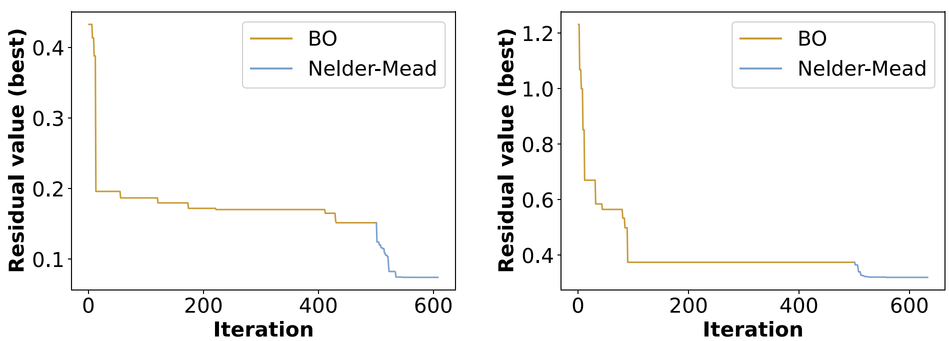

(**a**) (**b**)

Figure 9: Residual value histories during Bayesian optimization and Nelder-Mead simplex algorithm refinement: (**a**) Tension; (**b**) Compression.

The final residual values for Bayesian optimization and Nelder-Mead simplex algorithm are documented in Table 6. In this table, we can qualitatively see that the Bayesian optimization provides a significant improvement in the optimization scheme.

Table 6: Residual values of Bayesian optimization (BO) and Nelder–Mead simplex method.

Specimen	Bayesian Optimization Initial	Bayesian Optimization Final	Nelder-Mead Simplex Final
Tension	0.4328	0.1517	0.0743
Compression	1.23181	0.3744	0.3201

3.3 Hyperparameter Tuning History

Figs. 10 and 11 present the histories of the Gaussian process kernel hyperparameters, amplitude scaling (s) and length scale (ℓ) for tension and compression, respectively. During the Bayesian optimization process, the marginal likelihood function in Eq. (27) reestimated the hyperparameters every 5 iterations. In the early phase (approximately the first 200 iterations), both tension and compression parameters show obvious variability. After the early phase, the parameter of tension stabilized around 2.5 and 0.4 for s and ℓ, while the compression parameters moved downward slightly. The hyperparameter tuning variation history pattern is also shown in the literature [23].

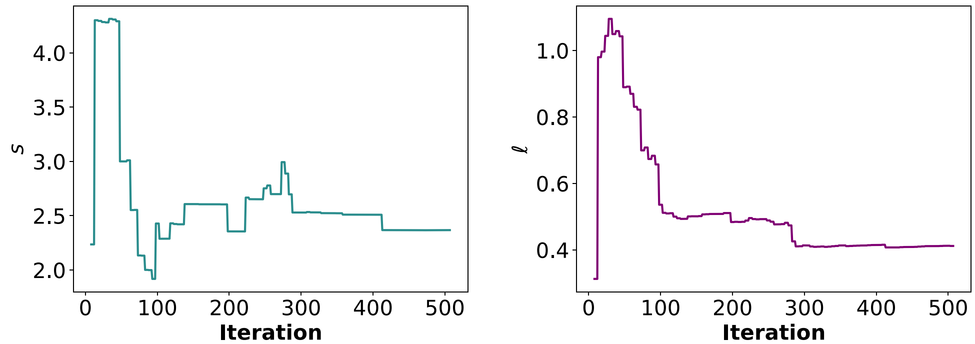

(**a**) (**b**)

Figure 10: History of tension specimen hyperparameter tuning: (**a**) Amplitude scaling (s); (**b**) Length scale (ℓ).

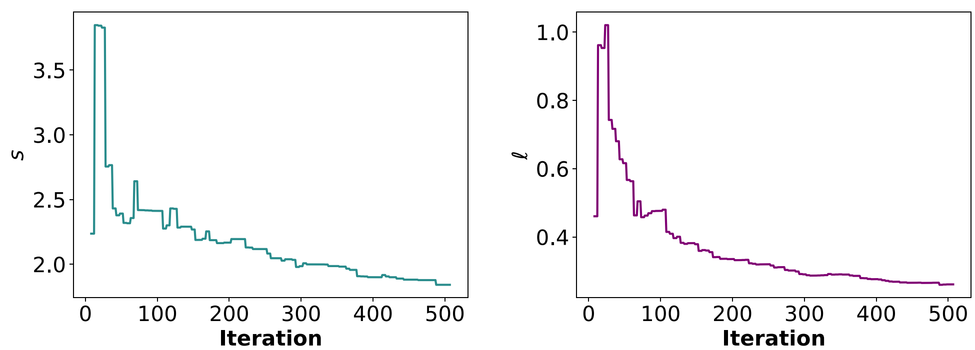

(**a**) (**b**)

Figure 11: History of compression specimen hyperparameter tuning: (**a**) Amplitude scaling (s); (**b**) Length scale (ℓ).

4 Discussion

This work demonstrated that the framework of using a polynomial-based strain hardening material model in plasticity calibrated by an online hyperparameter Bayesian optimization scheme can effectively capture the plastic deformation behavior of Ti-6Al-4V under both tension and compression. The good agreement between experimental and numerical force–displacement responses was obtained. In this section, the significance of our findings is discussed.

The identified yield stress-effective plastic strain behavior highlights the different strain hardening characteristics of Ti-6Al-4V for tension and compression. The stress vs. strain response displays a clear nonlinear behavior. In tension, it starts with a high initial modulus, followed by a gradual decrease in modulus, but still greater than zero. In contrast, the stress vs. strain shows a more linear response within the examined region in compression. This difference is consistent with experimental observations reported in the literature and reflects the inherent tension and compression asymmetry of Ti-6Al-4V [15], which is often attributed to microstructural mechanisms. To be specific, Ti-6Al-4V is a two-phase (α and β) alloy, which makes it deform not in the same way [43–46]. At the crystal level, different deformation mechanisms are activated under tension and compression, leading to different macroscopic stress–strain responses [43–45].

It should be noted that the present study was conducted using the available quasi-static experimental data under constant loading conditions at room temperature. Therefore, the effects of different strain rates and testing temperatures were not investigated in the current model calibration. Since Ti-6Al-4V can show strain-rate and temperature-dependent plastic deformation behavior, additional experimental data under different loading rates and thermal conditions are required to further evaluate the generalizability of the proposed model. In addition, the current framework was applied to uniaxial tension and compression tests along the rolled material direction. More complex stress states and direction-dependent material behaviors associated with different specimen orientations were not considered in the present work. These limitations indicate that the current model should not be regarded as a complete constitutive description for all possible deformation modes of Ti-6Al-4V.

As for the fitting deviation in the yield region of the compression curve, this is not only attributed to initial guess limitations. It can also be caused by the optimization algorithm. Bayesian optimization is trying to find a global solution for the full stress–strain response. Therefore, the final fit represents a compromise for the entire curve rather than the points in every local region. In addition, the relatively sharp transition in the compression yield region may be difficult to fully capture using the adopted polynomial-based model.

The optimization histories demonstrate that the optimization scheme provides an efficient global search to identify the strain hardening parameters. The rapid reduction of the residual values by Bayesian optimization indicates that this Gaussian process surrogate model can guide the search direction successfully. Compared with conventional methods such as grid search, gradient-based optimization, and genetic [21] algorithms, our Bayesian optimization enhanced by online hyperparameter tuning, as recorded in Figs. 10 and 11, shows its efficient capacity to reduce the residual. It is important to recognize that genetic algorithm, as an evolutionary approach, typically require a large number of sampling points during the iterative search process [47]. Thus, it is often feasible for analytical or computationally inexpensive problems. However, it may become impractical for inverse finite element analysis involving realistic three-dimensional geometries and complex boundary conditions. The benefit of the online hyperparameter scheme is also demonstrated and discussed in the literature [23]. In addition, the subsequent local refinement by the Nelder–Mead method effectively improves the solution. This demonstrates the benefit of combining global and local optimization strategies.

Thus, they are often feasible for analytical or computationally inexpensive problems, but may become impractical for inverse finite element analysis involving realistic three-dimensional geometries and complex boundary conditions.

The hyperparameters fluctuated more significantly in the early iterations. As additional sample points were collected during later iterations, the uncertainty was gradually reduced and then the hyperparameters became more stable. This trend can be considered as a qualitative indicator that the optimization process is entering a more stable stage. However, hyperparameter stabilization alone should not be interpreted as a strict proof of convergence to the global optimum.

5 Conclusion

This work proposes a computational framework for identifying the strain-hardening plasticity model of titanium alloy Ti-6Al-4V under both tensile and compressive loading. A rational polynomial–based strain hardening model is adopted and calibrated using force–displacement responses from experiment. It offers a flexible representation of the nonlinear strain hardening plastic behavior. In addition, this work represents the first application of Bayesian optimization with online hyperparameter tuning to identify strain hardening parameters of Ti-6Al-4V under tension and compression.

Future work should include additional experiments to better quantify the variability and uncertainty associated with Bayesian calibration. Further simulation studies are also needed to assess the applicability and limitations of the proposed material model for force–displacement responses up to failure points. In addition, the effect of the hyperparameter tuning interval should be systematically investigated to further improve the optimization framework. The element formulation sensitivity and hourglass control are also worth testing. Finally, further investigations under various loading conditions, such as different strain rates, temperatures, bending, and torsion, together with direction-dependent material behaviors, are needed to fully develop, evaluate, and validate the proposed material model.

Acknowledgement: Not applicable.

Funding Statement: The authors received no specific funding for this study.

Author Contributions: The authors confirm contribution to the paper as follows: Conceptualization, Teng Long and Leyu Wang; methodology, Teng Long and Leyu Wang; software, Leyu Wang; validation, Teng Long and Leyu Wang; formal analysis, Teng Long and Leyu Wang; writing—original draft preparation, Teng Long and Leyu Wang; writing—review and editing, Teng Long, Leyu Wang, Cing-Dao Kan and James D. Lee; visualization, Teng Long and Leyu Wang; supervision, Leyu Wang and James D. Lee; project administration, Leyu Wang, Cing-Dao Kan and James D. Lee. All authors reviewed and approved the final version of the manuscript.

Availability of Data and Materials: The data that support the findings of this study are available from the Corresponding Author, [Leyu Wang], upon reasonable request.

Ethics Approval: Not applicable.

Conflicts of Interest: The authors declare no conflicts of interest.

References

1. Aghaahmadi M, Kim WH, Lee H, Choi MS, Kim JS, Kim JH. Optimization of 75 mm ultra-thick Ti-6Al-4V alloy plates for aerospace applications: microstructure and mechanical properties analysis. Mat Transact. 2025;66(5):590–9. doi:10.2320/matertrans.mt-mc2024007.
2. Cai Y, Song Y, Dong K, Liu X, Han EH. Threshold potential for hydrogen-induced damage of Ti-6Al-4V alloy under deep-sea environment: a mechanistic insight. Acta Mater. 2025;304:121792. doi:10.1016/j.actamat.2025.121792.
3. Takahashi K, Mori K, Takebe H. Application of titanium and its alloys for automobile parts. MATEC Web Conf. 2020;321(2):02003. doi:10.1051/matecconf/202032102003.
4. Mukhtar Z, Dey A, Kundan N. Optimized surface engineering of Ti-6Al-4V: comprehensive coating evaluation for biomedical applications. Surf Interf. 2025;56:105735.
5. Zhao R, Zhang Z, Chen H, Han J, Ren Z, Zhang C, et al. Achieving heterogeneous microstructure and enhanced strength-ductility synergy in Ti-6Al-4V titanium alloy via corrugated-flat rolling process. Mat Sci Eng A. 2025;933:148260. doi:10.1016/j.msea.2025.148260.
6. Lu F, Ma Q, Liu E, Wei R, Bai J, Gao Q, et al. Advancements in understanding the microstructure and properties of additive manufacturing Ti-6Al-4V alloy: a comprehensive review. J Alloys Comp. 2025;1027(10):180543. doi:10.1016/j.jallcom.2025.180543.
7. Gurrappa I. Characterization of titanium alloy Ti-6Al-4V for chemical, marine and industrial applications. Mater Charact. 2003;51(2–3):131–9. doi:10.1016/j.matchar.2003.10.006.
8. Li H, Wang Y, Zhu J, Liu Y, Wang Q, Chen Y, et al. Micro-plastic deformation behavior and life enhancement mechanism of additively manufactured Ti-6Al-4V titanium alloy during high cycle fatigue. Int J Fatigue. 2025;201:109170. doi:10.1016/j.ijfatigue.2025.109170.
9. Knott B, Wang L, White E, Seidt J, Gilat A, Carney K, et al. Ductile fracture of 2024-T351 aluminum and Ti-6al-4v under plane strain compression. SSRN Electron J. 2025. doi:10.2139/ssrn.5202775.

10. Wang S, Zhao X, Huo J. Impact of a bird strike on the aerodynamic performance and damage behavior of a full-scale aeroengine fan. Aerosp Sci Technol. 2024;151(1):109270. doi:10.1016/j.ast.2024.109270.
11. Janda A, Ralph BJ, Demarty Y, Sorger M, Ebenbauer S, Prestl A, et al. Ballistic tests on hot-rolled Ti-6Al-4V plates: experiments and numerical approaches. Def Technol. 2023;26(1–2):39–53. doi:10.1016/j.dt.2022.11.012.
12. Hammer JT, Yatnalkar RS, Seidt JD, Gilat A. Plastic deformation of Ti-6Al-4V plate over a wide range of loading conditions. In: Dynamic behavior of materials, Volume 1: Proceedings of the 2012 Annual Conference on Experimental and Applied Mechanics. Cham, Switzerland: Springer; 2012. p. 165–9.
13. Long T, Wang L, Lee JD, Kan CD. Temperature effects on critical energy release rate for aluminum and titanium alloys. Symmetry. 2024;16(2):142. doi:10.3390/sym16020142.
14. Niu W, Mo R, Sun H, Gnanasekaran B, Zhu Y, Liu G. A smooth particle hydrodynamic model for two-dimensional numerical simulation of Ti-6Al–4V serrated chip deformation based on TANH constitutive law. Proc Inst Mech Eng Part C J Mech Eng Sci. 2019;233(9):3004–17. doi:10.1177/0954406218803981.
15. Haight S, Wang L, Du Bois P, Carney K, Kan CD. Development of a titanium alloy Ti-6Al-4V material model used in LS-DYNA DOT. Washington, DC, USA: Federal Aviation Administration; 2016.
16. Yatnalkar RS. Experimental investigation of plastic deformation of Ti-6Al-4V under various loading conditions [master's thesis]. Columbus, OH, USA: The Ohio State University; 2010.
17. Hammer JT. Plastic deformation and ductile fracture of Ti-6Al-4V under various loading conditions [master's thesis]. Columbus, OH, USA: The Ohio State University; 2012.
18. Platen J, Storm J, Kaliske M. Utilization of the quadratic hill yield function to model Ti-6Al-4V within multiplicative finite strain kinematics. Int J Eng Sci. 2025;213:104268. doi:10.1016/j.ijengsci.2025.104268.
19. Chen X, Zhang B, Du Y, Liu M, Bai R, Si Y, et al. Constitutive model parameter identification based on optimization method and formability analysis for Ti6Al4V alloy. Materials. 2022;15(5):1748. doi:10.3390/ma15051748.
20. Sedighi M, Khandaei M, Shokrollahi H. An approach in parametric identification of high strain rate constitutive model using Hopkinson pressure bar test results. Mat Sci Eng A. 2010;527(15):3521–8. doi:10.1016/j.msea.2010.02.025.
21. Chen X, Su Z, Sun J, Yang Z, Zhang B, Zhou Z. Genetic-algorithm-based inverse optimization identification method for hot-temperature constitutive model parameters of Ti6Al4V alloy. Materials. 2023;16(13):4726. doi:10.3390/ma16134726.
22. Papenmeier L, Cheng N, Becker S, Nardi L. Exploring exploration in bayesian optimization. arXiv:2502.08208. 2025.
23. Long T, Wang L, Kan CD, Lee JD. Online hyperparameter tuning in bayesian optimization for material parameter identification: an application in strain-hardening plasticity for automotive structural steel. AppliedMath. 2026;6(1):6.
24. Seidt JD, Gilat A. Plastic deformation of 2024-T351 aluminum plate over a wide range of loading conditions. Int J Solids Struct. 2013;50(10):1781–90. doi:10.1016/j.ijsolstr.2013.02.006.
25. Hallquist JO. LS-DYNA keyword user's manual. Livermore Softw Technol Corporat. 2007;970:299–800.
26. Long T, Wang L, Kan CD, Lee JD. A novel approach for modeling strain hardening in plasticity and its material parameter identification by bayesian optimization for automotive structural steels application. AppliedMath. 2025;5(3):104. doi:10.3390/appliedmath5030104.
27. Casey J. On elastic-thermo-plastic materials at finite deformations. Int J Plast. 1998;14(1–3):173–91. doi:10.1016/s0749-6419(97)00047-8.
28. Chen Y, Lee JD, Eskandarian A. Meshless methods in solid mechanics. Vol. 9. Cham, Switzerland: Springer; 2006.
29. Lee JD, Li J. Advanced continuum theories and finite element analyses. Vol. 2. Singapore: World Scientific; 2020.
30. Green AE, Naghdi PM. A general theory of an elastic-plastic continuum. Berkeley, CA, USA: University of California; 1964.
31. Shawe-Taylor J, Cristianini N. Kernel methods for pattern analysis. Cambridge, UK: Cambridge University Press; 2004.

32. De Ath G, Fieldsend JE, Everson RM. What do you mean? The role of the mean function in bayesian optimisation. In: Proceedings of the 2020 Genetic and Evolutionary Computation Conference Companion. New York, NY, USA: ACM; 2020. p. 1623–31.
33. De Ath G, Everson RM, Rahat AA, Fieldsend JE. Greed is good: exploration and exploitation trade-offs in Bayesian optimisation. ACM Trans Evolution Learn Optimiz. 2021;1(1):1–22.
34. Hernández-Lobato JM, Hoffman MW, Ghahramani Z. Predictive entropy search for efficient global optimization of black-box functions. In: NIPS'14: Proceedings of the 28th International Conference on Neural Information Processing Systems. Cambridge, MA, USA: MIT Press; 2014. p. 918–26.
35. Drew Bagnell CMU. Statistical techniques in robotics-machine learning and probabilistic approaches to uncertainty and adaptation. 2014 [cited 2026 May 10]. Available from: https://www.cs.cmu.edu/.
36. Gabriele Farina MIoT. Lecture 16, Bayesian optimization. 2024 [cited 2026 May 10]. Available from: https://www.mit.edu/~gfarina/2024/67220s24_L16_bayesian_optimization/.
37. Duvenaud D. Automatic model construction with Gaussian processes [dissertation]. Cambridge, UK: University of Cambridge; 2014.
38. Rasmussen CE, Williams CKI. Gaussian processes for machine learning. Cambridge, MA, USA: MIT Press; 2005.
39. Schnabel RB, Eskow E. A new modified Cholesky factorization. SIAM J Scient Statist Comput. 1990;11(6):1136–58. doi:10.1137/0911064.
40. Nelder J, Mead R. A simplex method for function minimization. Comput J. 1965;7(4):308–13. doi:10.1093/comjnl/7.4.308.
41. Lagarias J, Reeds J, Wright M, Wright P. Convergence properties of the nelder-mead simplex method in low dimensions. SIAM J Optimiz. 1998;9(1):112–47. doi:10.1137/s1052623496303470.
42. Jones E, Oliphant T, Peterson P. SciPy: open source scientific tools for Python. 2001 [cited 2026 May 10]. Available from: http://www.scipy.org/.
43. Neeraj T, Savage M, Tatalovich J, Kovarik L, Hayes R, Mills M. Observation of tension-compression asymmetry in α and titanium alloys. Philos Mag. 2005;85(2–3):279–95. doi:10.1080/14786430412331315707.
44. Warwick J, Coakley J, Raghunathan S, Talling R, Dye D. Effect of texture on load partitioning in Ti-6Al-4V. Acta Materialia. 2012;60(10):4117–27. doi:10.1016/j.actamat.2012.03.039.
45. Suryawanshi J, Singh G, Msolli S, Jhon MH, Ramamurty U. Tension-compression asymmetry and shear strength of titanium alloys. Acta Mater. 2021;221:117392. doi:10.1016/j.actamat.2021.117392.
46. Hémery S, Villechaise P, Banerjee D. Microplasticity at room temperature in α/β titanium alloys. Metall Mat Trans A. 2020;51(10):4931–69. doi:10.1007/s11661-020-05945-4.
47. Jin Y. A comprehensive survey of fitness approximation in evolutionary computation. Soft Comput. 2005;9(1):3–12. doi:10.1007/s00500-003-0328-5.